

## Article

# Geotechnical Investigations and Support Design for an Underground Powerhouse of Pumped-Storage Power Station: A Case Study in Chongqing, China

Qiang Zhang <sup>1,2</sup>  and Yanni Zheng <sup>1,\*</sup><sup>1</sup> School of Civil Engineering, Central South University, Changsha 410075 China; zhangq@iwhr.com<sup>2</sup> China Institute of Water Resources and Hydropower Research, Beijing 100048, China

\* Correspondence: zhengyanni710082@126.com

**Abstract:** This study assesses the efficiency of the empirically recommended supported design of the underground powerhouse of the Panlong pumped-storage power station in Chongqing, China by using 3D distinct element code (3DEC). Field and laboratory tests were conducted to investigate the geological properties of intact rock and rock mass. The results showed that the stability of the large powerhouse may be controlled by the soft rock (mudstone) layers. The rock mass was classified in terms of the Q classification system, basic quality (BQ) method, and hydropower classification (HC) method, and then the supported system was put forward. The efficiency of the designed supported was checked based on the numerical simulation results of deformation and plastic zone. The results showed that the installed support reduces the radius of the plastic zones and the maximum deformation significantly.

**Keywords:** underground powerhouse; rock mass classification; numerical modeling; empirical approach; support systems; surrounding rock



**Citation:** Zhang, Q.; Zheng, Y. Geotechnical Investigations and Support Design for an Underground Powerhouse of Pumped-Storage Power Station: A Case Study in Chongqing, China. *Sustainability* **2022**, *14*, 8481. <https://doi.org/10.3390/su14148481>

Academic Editors: Jianjun Ma, Mingfeng Lei, Yu Liang and Yuexiang Lin

Received: 23 May 2022

Accepted: 8 July 2022

Published: 11 July 2022

**Publisher's Note:** MDPI stays neutral with regard to jurisdictional claims in published maps and institutional affiliations.



**Copyright:** © 2022 by the authors. Licensee MDPI, Basel, Switzerland. This article is an open access article distributed under the terms and conditions of the Creative Commons Attribution (CC BY) license (<https://creativecommons.org/licenses/by/4.0/>).

## 1. Introduction

During the construction of an underground structure, the stability control of cavern surrounding rock is the primary scientific issue [1]. How to effectively control the harmful deformation and catastrophic damage of rock masses through scientific, reasonable, and economically reliable excavation and support optimization methods is an unavoidable technical problem for large-scale underground engineering construction. The stability of the underground structure is affected by external and internal factors such as mechanical properties of rock mass, structural, in-situ stress, groundwater, excavation geometries, and safety requirements [2,3]. Empirical and numerical methods are widely used to access these parameters for supporting underground structures [4]. Based on the practice of civil, transportation, hydropower, and mining engineering, different rock mass classification systems have been developed and they are considered power tools for supporting the design of the underground structure. The commonly used systems are rock structure rating (RSR) [5], rock mass rating (RMR) [6], Q system [7], basic quality (BQ) [8], hydropower classification (HC) [9], et. al.

However, rock classification methods do not provide the plastic zone thickness and stress distribution around the excavation opening zone. Particular attention should be paid when using these subjective methods. On the other hand, the numerical approaches no matter continuum or discontinue modeling have the advantage of simulating ground complexities, such as the sophisticated geometries, the high in-situ stress, the abundant groundwater, and the interaction between surrounding rock mass and supporting structures. Xing et al. [10,11] studied the support of an underground mine in rock mass containing large discontinuities with the global reinforcement model in 3DEC. Yang et al. [12] investigated the deformation, stress, and crack evolution characteristics of the roadway

under unsupported and primary support conditions. A new “bolt-cable-mesh-shotcrete + shell” combined support was developed to handle the large deformation of the roadway. Kanik and Gurocak [13] analyzed the support elements of the Macka tunnel with the Finite Elements Method (FEM). It shows that the optimum support systems are compatible with the support system recognized by the RMI rock mass classification systems. Moreover, the numerical approach can improve the understanding and evaluation of failure mechanisms, geotechnical risks, and the construction of more effective rock reinforcement systems [14,15].

Even though numerous numerical analyses have been performed on the stability assessment and support design for underground structures as mentioned above, the majority of the studies only considered the impact of a single engineering or geological factor or simply used two-dimensional (2D) modeling. The stability of excavations is significantly impacted by the 3D redistribution of excavation-induced stresses, which is a three-dimensional (3D) problem in the behavior of subterranean excavation in rock masses. For precise rock mass behavior prediction in numerical modeling, it is essential to simulate the 3D sequences of excavation and rock support. A 2D analysis or a 3D analysis that has been greatly simplified could produce numerical results that are not accurate to reality. The geology conditions of the underground structure are usually complicated. The conventional FEM cannot simulate the deformation of excavation underground with many soft rock layers well.

In the paper, the main powerhouse of the Panlong pumped-storage power station was selected as an implementation site for the empirical and numerical design of support of the underground structure. Field and laboratory tests followed empirical rock mass classification and numerical modeling was performed to determine the efficacy of the design support.

## 2. Geology Investigation of the Underground Powerhouse

The Panlong Pumped-storage Power Station is located in Zhongfeng Town, Qijiang District, southwest of Chongqing, about 80 km away from the main urban area of Chongqing. The power station has an installed capacity of 1200 MW. After the power station is completed, it will undertake the tasks of peak regulation, valley filling, frequency regulation, phase regulation, and accident backup of Chongqing’s power grid. It will be an important backbone power source in Chongqing’s future power grid. The pivotal project is mainly composed of buildings such as upper and lower reservoirs and water transmission and power generation systems.

The location of the underground powerhouse of the Panlong pumped-storage power station is presented in Figure 1. The underground powerhouse adopts a rear-end layout, and the main buildings include the main powerhouse, headrace tunnel, and pressure shaft, and tailrace tunnel. The longitudinal axis direction of the main powerhouse is N80°W, and the excavation size is 171.00 × 25.00 × 52.425 m (length × width × height). The two large caverns of the main powerhouse and the main transformation tunnel are 55 m apart and arranged in parallel. The installation site is located at the right end of the main plant. The ground auxiliary plant, switch station, and outlet yard are arranged together. It is located on the right bank of Wangjiawujigou in the upper reaches of Lianghekou, about 150 m away from the inlet/outlet of the lower reservoir.

The project is located at the northeast wing of the Zhongfengsi syncline (axial northwest) and the southeast wing of the Huajinshan syncline (axial northeast). According to the engineering geological cross-section drawing of the main underground powerhouse (Figure 2), the exposed strata are the Mesozoic Jurassic Upper Penglaizhen Formation ( $J_{3p}$ ) and Cretaceous Upper Jiaguan Formation ( $K_{2j}$ ), and the unevenly distributed Quaternary loose accumulation. The lithology of the underground powerhouse area in the middle and lower-middle and lower part of the Jiaguan Formation ( $K_{2j}^{1-1}$ ) middle and fine-grained sandstone, gravelly coarse sandstone, conglomerate intercalated with argillaceous siltstone and silty mudstone, and the second member of the Penglaizhen Formation. The top of the

section ( $J_{3p}^{2-3}$ ) is purple-gray, gray-green sandstone, siltstone, argillaceous siltstone, and mudstone. The elevation of the boundary between the two is 473.59–469.90–479.82 m from south to north. The main and auxiliary powerhouse caverns above the bus bar layer are the Jiaguan group stratum, and the installation elevation (466.00 m) below is the Penglaizhen group stratum.

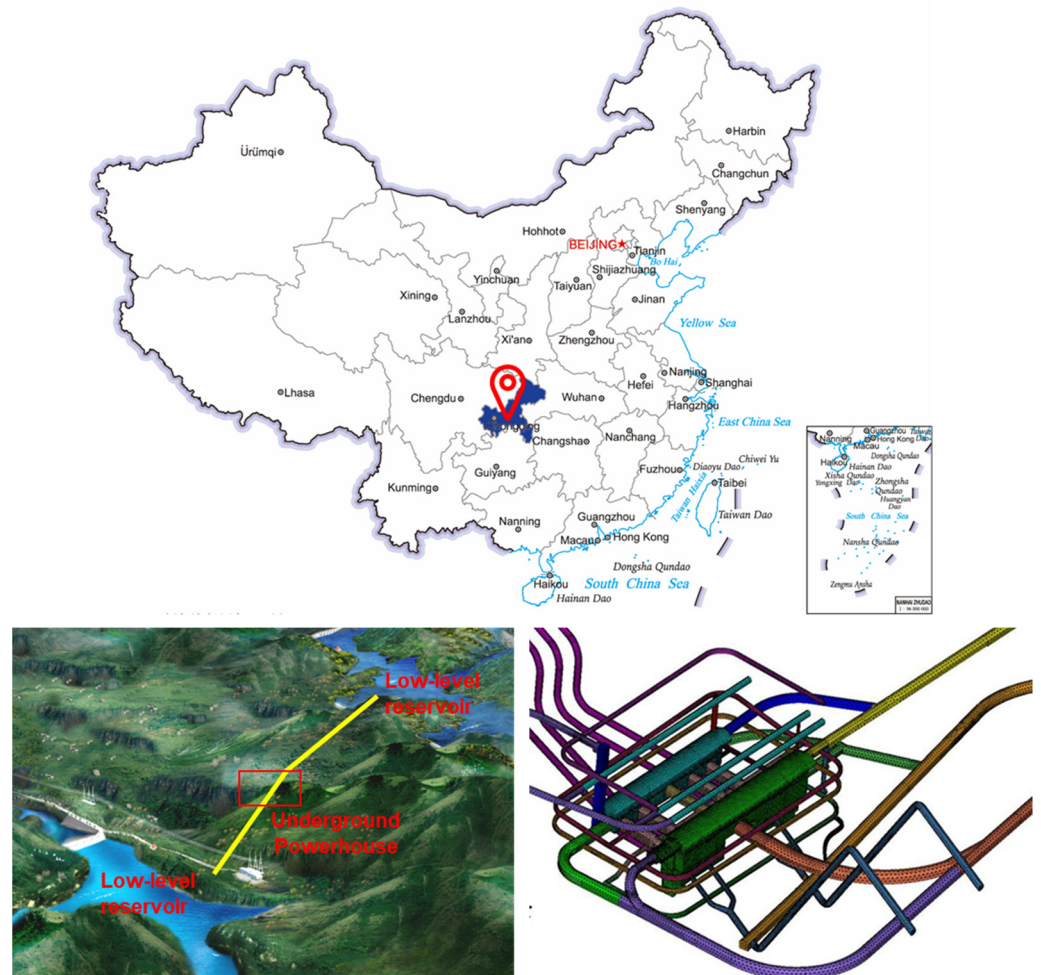


**Figure 1.** The location of the underground powerhouse of the Panlong pumped-storage power station [16].

The geological structure of the main underground powerhouse is simple and there are no regional faults and large-scale faults passing through the study area. According to the statistics of exploring caves in the underground powerhouse area, the main structural planes are rock layers and joint cracks. The rock layers are gentle, and the orientations are mainly with a strike of  $N15^{\circ}$ – $25^{\circ}$ W and a dip angle of  $4$ – $10^{\circ}$ . Each group of joint cracks in the project area is dominated by steep dip angles, with straight faces and longer extensions, which are mainly developed in medium to thick sandstones. The joints in siltstone and conglomerate are short, small, and undeveloped. Four main joint cracks develop with the following attitudes: (1) a strike of  $N50^{\circ}$ – $70^{\circ}$ W, a tendency of SW and a dip angle of  $60$ – $85^{\circ}$ , (2) a strike of  $N70^{\circ}$ – $90^{\circ}$ W, a tendency of SW and a dip angle of  $50$ – $85^{\circ}$ , (3) a strike of  $N30^{\circ}$ – $50^{\circ}$ W, a tendency of SW and a dip angle of  $60$ – $80^{\circ}$ , (4) a strike of  $N65^{\circ}$ – $85^{\circ}$ E, a tendency of SE and a dip angle of  $70$ – $85^{\circ}$ . Figure 3 shows the rose diagram and stereographic projection of the joints and fissures in the plant area. There are 386 joints with a length of more than 1 m, the development density is 0.42/m, and the spacing is 2.4 m. The joints are mostly closed, with local micro-opening and no filling.

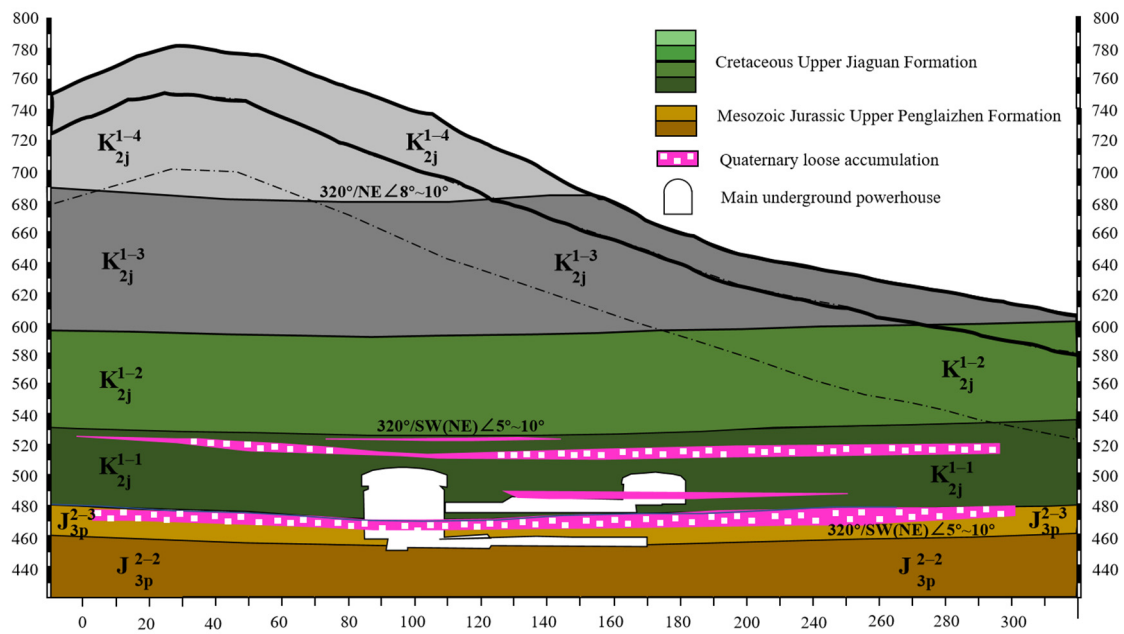


Figure 2. Engineering geological cross-section drawing of the main underground powerhouse.

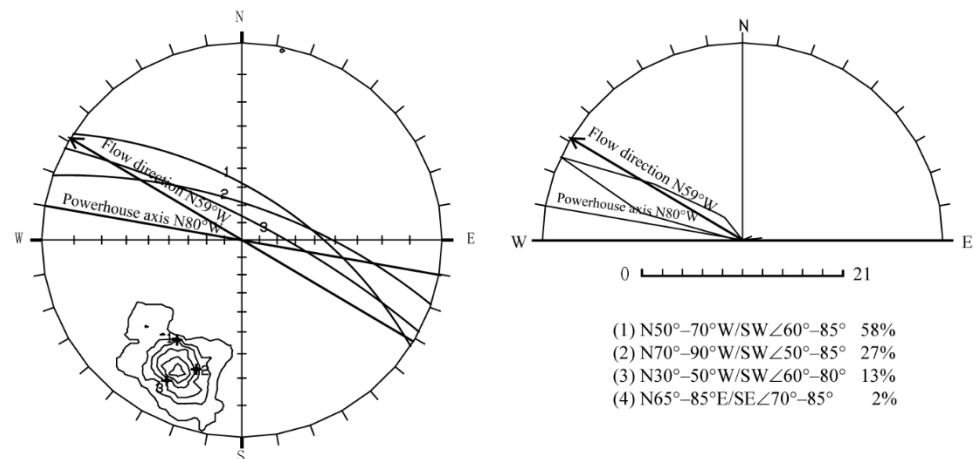
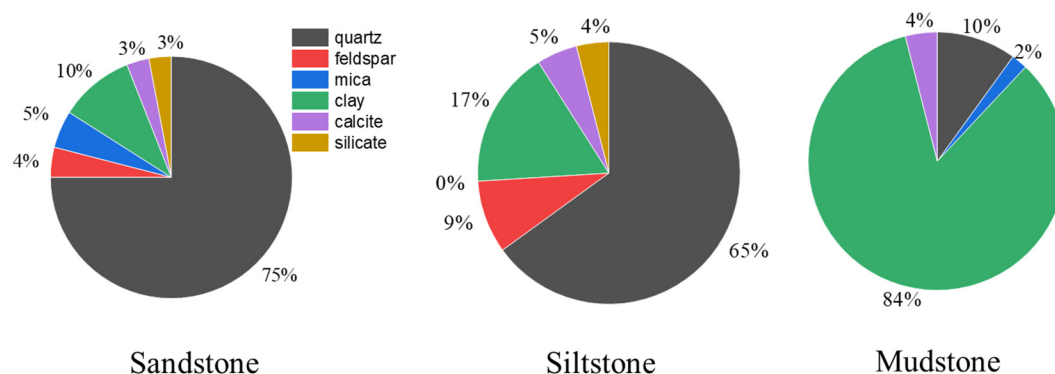


Figure 3. Stereographic projection of the main geological structures in the main underground powerhouse.

In summary, the lithology of rock in the project area is sandstone, siltstone, mudstone, conglomerate, etc. The main factors affecting the engineering geological characteristics of rock masses are the mineral composition of the rock, mechanical strength of rock, weathering degree; development and mechanical properties of structural planes in the rock mass, integrity and deformation characteristics of rock mass; in situ stress state and groundwater characteristics, etc. Therefore, in-situ and laboratory tests were carried out to identify the physical and mechanical properties of the rocks. Details are shown as follows.

To evaluate the mineral composition of rocks, X-ray diffraction (XRD) analyses of the powdered rock were conducted in the laboratory, and the results are shown in Figure 4. Sandstone and siltstone are mainly composed of quartz while mudstone is dominated by clay. Particularly, Clay minerals are mainly composed of chlorite and montmorillonite mixed-layer minerals and illite and montmorillonite mixed-layer minerals which means that mudstone has a certain degree of expansion and contraction. However, the sandstone and siltstone are more brittle due to the existence of quartz.



**Figure 4.** Mineral composition of the typical rock in the underground powerhouse area.

Laboratory tests were performed on the core samples prepared from the drilling based on the methods suggested by ISRM [17]. The physical and mechanical properties including unit weight, porosity, uniaxial compressive strength, tensile strength, softening coefficient, Young's modulus, and Poisson's ratio were investigated. Moreover, the rock quality designation (RQD) was determined from the drillings and scan-line surveys based on the method proposed by Priest and Hudson [18] (Table 1). Most of the rock porosity in the underground powerhouse is about 6%. The saturated compressive strength  $R_c$  of sandstone is 41.7–113.0 MPa, with an average value of 68.4 MPa, and is dominated by hard rock. The  $R_c$  of siltstone is 34.4–42.6 MPa, with an average value of 38.5 MPa, and belongs to medium-hard rock. The saturated compressive strength of the conglomerate is 23.5–35.2 MPa, and the average value is 31.6 MPa, which belongs to medium-hard rock. The saturated compressive strength of mudstone is 4.48–16.0 MPa, and the average value is 8.80 MPa, which is belong to soft rock.

**Table 1.** Physical and mechanical properties of intact rock.

Lithology	Unit Weight (kN/m <sup>3</sup> )	Porosity (%)	$R_c$ (MPa)	$T_c$ (MPa)	$E$ (GPa)	$\nu$	RQD
Sandstone	(24.6–26.6) 25.1	(2.97–6.46) 5.02	(41.7–113.0) 68.4	(0.73–2.44) 1.23	(14.5–31.4) 22.7	(0.22–0.30) 0.27	97
conglomerate	(26.2–26.5) 26.3	(2.26–2.62) 2.44	(23.5–35.2) 31.6	(0.91–2.08) 1.22	(12.6–24.9) 19.2	(0.21–0.28) 0.24	90
Siltstone	(25.4–26.1) 25.8	8.79	(34.4–42.6) 38.5	–	(14.5–17.8) 16.5	(0.29–0.30) 0.30	86
Mudstone	(25.9–26.1) 26.1	6.27	(4.48–16.0) 8.80	(1.07–1.89) 1.11	(12.9–17.3) 15.7	0.26	80

As the strength of mudstone is much lower, the mechanical properties of the structural plane between mudstone and sandstone or concrete control the stability of the underground powerhouse. Therefore, the in-situ shear tests were conducted in the exploration adits followed by the method suggested by ISRM [17] to study the shear strength of the structural plane. Five samples were tested, and the results are shown in Figure 5 (Figure 5a is the structural planes between mudstone and sandstone, and Figure 5b is the structural planes between mudstone and concrete). The cohesion and friction angle of mudstone are sandstone is 0.17 MPa and 21.5°, respectively. The cohesion and friction angle of the structural plane between mudstone and concrete are 0.54 MPa and 21.5° according to the linear fitting results. However, we find that the logarithmic function can describe the shear strength of the structural plane between mudstone and concrete better. We can see that the cohesion of the structural plane between mudstone and sandstone is extremely low.

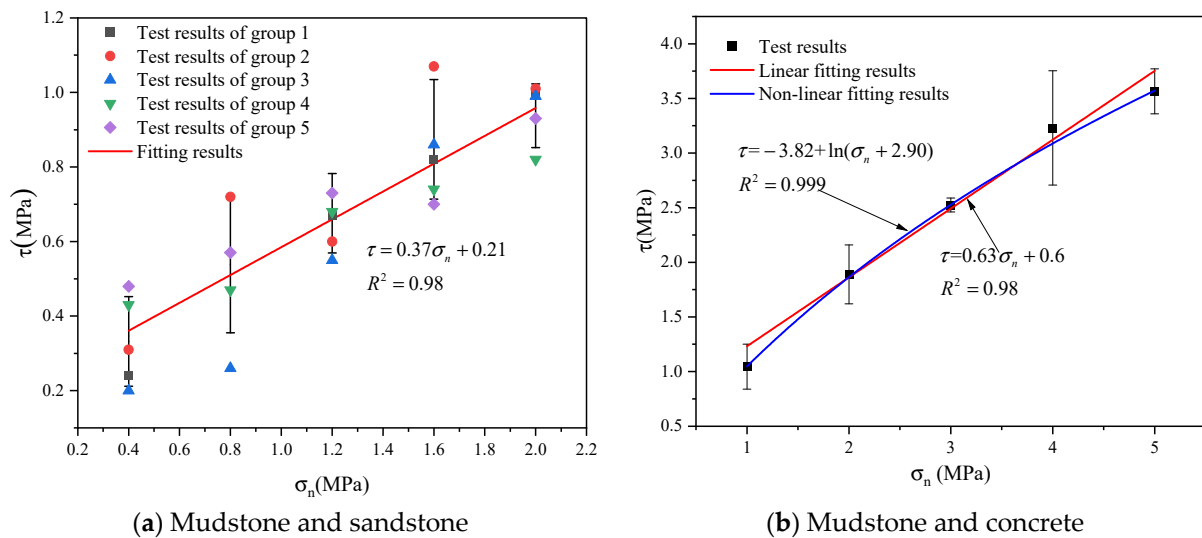


**Figure 5.** In situ shear tests of the structural plane between mudstone and (a) sandstone and (b) concrete.

The deformation moduli  $E_m$  of the rock masses were calibrated through the rigid bearing plate method suggested by the Ministry of Land and Resources [19]:

$$E_m = \frac{pb(1 - \mu_m^2)\omega}{W} \quad (1)$$

where  $p$  is the pressure applied on the rigid bearing plate, MPa,  $b$  is the diameter of the plate, cm,  $W$  is the total deformation of rock mass, cm,  $\omega$  is a coefficient related to the stiffness and shape of the rigid bearing plate, in this paper,  $\omega = 0.785$  according to the Chinese National Standard GB/T 50266-2013 (2013).  $\mu_m$  is the Poisson's ratio of the rock mass. 28 tests were conducted in situ and the results showed that the average deformation modulus of sandstone, conglomerate and siltstone are 14.9, 6.55, and 6.71 GPa, respectively. In addition, the determined deformation moduli change little in horizontal and vertical directions, suggesting that the anisotropy of sandstone is not obvious. It should be noted that the deformation modulus of mudstone was not conducted due to the limitation of such rock mass. Therefore, it was determined by the following equation [20]:

$$E_m = E \left( 0.02 + \frac{1 - D/2}{1 + e^{(60+15D-GSI)/11}} \right) \quad (2)$$

where  $GSI$  is the geological strength index, and  $D$  is a coefficient describing the disturbance degree of the rock mass subject to blast damage and stress relaxation. It can be determined according to the method suggested by Hoek and Brown [21]. Details of these two parameters are given in Section 4.

Due to the existence of discontinuities and filling materials in the rock mass, the P-wave velocity of rock mass is slower than that of intact rock. Therefore, the relationship between initial p-wave velocity and the reduced p-wave velocity is widely used to reflect the physical and mechanical properties of the rock mass. The Poisson's ratio  $\mu_m$  of rock mass was measured through the seismic reflection method suggested by (Bowles, 1988). With the determined seismic vertical wave velocity ( $v_{pm}$ ) and horizontal wave velocity ( $v_{sm}$ ), the Poisson's ratio can be expressed as,

$$\mu_m = \frac{v_{pm}^2 - 2v_{sm}^2}{2(v_{pm}^2 - v_{sm}^2)} \quad (3)$$

The wave velocity of the rock mass can be identified through acoustic test methods such as the single-hole method, cross-hole method, and hammering method [22]. As the acoustic test results are significantly influenced by drilling direction, the cross-hole method was conducted to determine the p-wave velocity of rock mass in the study area and the typical results are given in Figure 6. The elastic wave CT in the underground powerhouse area shows that the wave velocity of the rock mass is mainly distributed between 3750–4500 m/s; the rock mass integrity is good. The area of wave velocity of 3000–3750 m/s is distributed in a gentle dip angle layer, and the distribution elevations are mainly 476.00–486.00 m, 516.00–526.00 m, and 456.00–466.00 m. Combined with borehole imaging results, it is caused by mudstone, argillaceous siltstone, and poorly cemented conglomerate. The borehole CT test results showed that the area of wave velocity less than 3000 m/s only accounted for 0.25% of the total scan area. It may be caused by joint fissures in the rock mass. The extremely low wave velocity area ( $V_p < 3000$  m/s) was not found in the borehole elastic wave CT scan area.

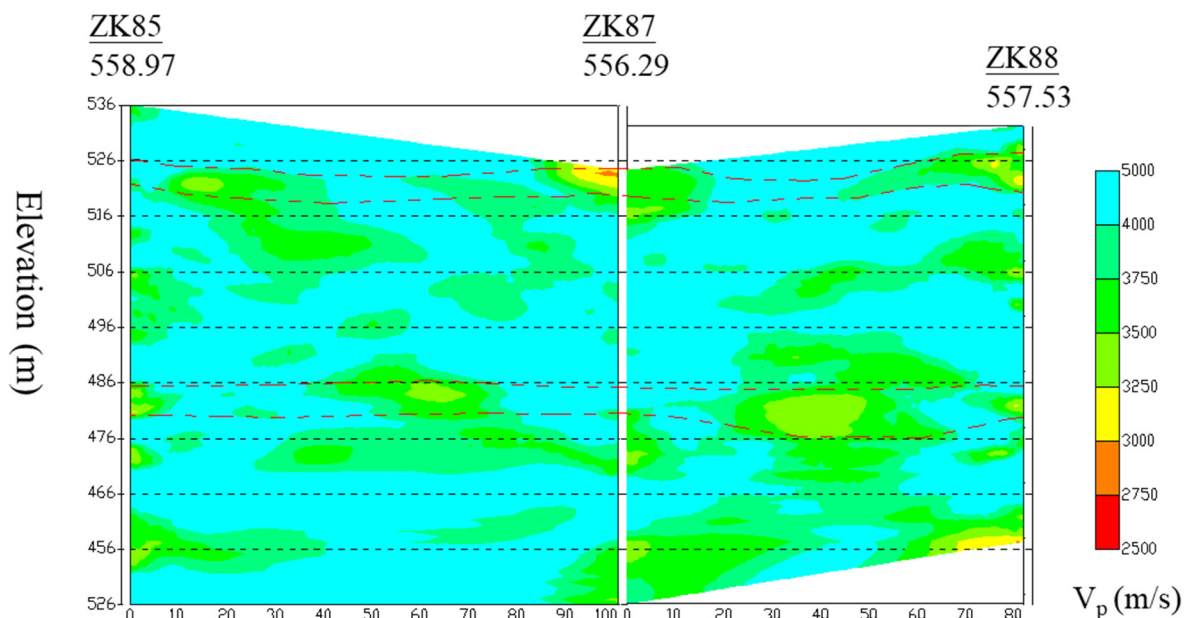


**Figure 6.** CT scanning section result of borehole elastic wave in underground powerhouse area.

It is generally accepted that in-situ stress has a significant influence on the stability of the underground structure. The stress relief method and hydraulic fracturing stress method are two widely used techniques to estimate the in-situ stress by ISRM [23]. Compared with the stress relief method, the hydraulic fracturing stress method does not have the limitation of the borehole depth and has lower excavation disturbance to the surrounding rock mass. Therefore, it was employed to estimate the in-situ stresses of the studied area. The results showed that the maximum principal stress of the underground powerhouse is between 5.47 MPa and 6.76 MPa, and the inclination angle is  $75.99\text{--}82.15^\circ$ , which is close to the vertical direction. The azimuth angle is  $103.90\text{--}116.69^\circ$ , and the overall performance is fluctuating in the east-west direction. The magnitude of the intermediate principal stress and the minimum principal stress is between 5.08–6.50 MPa and 3.84–5.02 MPa, respectively, the inclination angles of the minimum principal stress are all small and close to the horizontal direction.

The theoretical calculation value of the self-weight stress within the elevation range of 472.00–528.00 m in the underground powerhouse ( $\gamma \cdot H$ ,  $\gamma$  is  $2.7 \times 10^4$  N/m<sup>3</sup>, the thickness of the overlying rock mass is between 227–283 m) is between 6.13 MPa and 7.64 MPa. The measured value of the stress component  $\sigma_z$  in the vertical direction is between 5.26 MPa and 6.5 MPa. It is obvious that the measured value is slightly lower than the theoretical

calculation value, but the measured value is consistent with the maximum principal stress value.

The groundwater in the plant area is mainly bedrock fissure water, and the water-bearing rock mass is sandstone. The groundwater level is 550.00–700.00 m, high in the north and low in the south, and it is discharged from the lower reservoir in Shijiagou. According to the results of the water transmission power generation system and underground powerhouse drilling water pressure test results and PD1 exploration of flat caves, there are no obvious signs of groundwater activity along the joint cracks. The water permeability of the rock mass is weak.

### 3. Rock Mass Classification and Support Method

In this paper, the Q, Basic Quality (BQ), and Hydropower Classification (HC) rock mass classification systems were used to quantitatively depict the rock mass quality of the underground powerhouse. The data used for rock mass classification were obtained from field and laboratory tests. After characterizing the rock mass quality, the support design is conducted according to the Chinese standard [9].

#### 3.1. Q Classification System

The Q classification method is a rock mass quality classification method proposed by Barton, Lien and Lunde [7] Barton et al. (1974). This classification method is to express the relationship between the six geological parameters that indicate the quality of the rock mass:

where  $J_n$  represents the number of joint sets. The more broken the rock mass, the larger the value.  $J_r$  is the joint roughness number,  $J_a$  is the joint alteration number,  $J_w$  is the joint water reduction factor and  $SRF$  is a stress reduction factor. Based on these six parameters, the Q value can be calculated as,

$$Q = \frac{RQD}{J_n} \cdot \frac{J_r}{J_a} \cdot \frac{J_w}{SRF} \quad (4)$$

The rock mass of the underground powerhouse of the pumped-storage power station was characterized by the Q system. The determined Q values are given in Table 2.

**Table 2.** Classification of rock masses.

Rock Type	Sandstone		Conglomerate		Siltstone		Mudstone		
Wave velocity (m/s)	3940–4800		3280–3750		2700–2900		2000–3050		
$R_c$ (MPa)	41.7–113.0		23.5–35.2		34.4–42.6		4.48–16.0		
$K_v$	0.77–1.0		0.33–0.72		0.36–0.42		0.2–0.46		
BQ	430		316		292.5		233		
BQ method	$K_1$	Dry	0.1	Wet	0.23	Wet	0.25	Wet	0.45
	$K_2$	53–67°	0.2	85°	0.1	80°	0.1	60°	0.3
	$K_3$	Medium Stress	0	Medium Stress	0	Medium Stress	0	Medium Stress	0
	[BQ]	400		283		357.5		158	
Classification	III		IV		IV		V		
Q system	RQD	97%	97	90%	90	86%	86	80%	80
	$J_n$	2 sets	6	2 set	4	1 set	3	2 sets	4
	$J_r$	Rough	1.5	Rough	1.5	Rough	1.5	Rough	1.5
	$J_a$	Closed	2	Closed	3	Closed	3	mud	8
	$J_w$	Wet	1	Wet	1	Wet	1	Wet	1
	SRF	Medium stress	1	Medium stress	1	Medium stress	1	Medium stress	1
	Q	12		11		14		3.75	
Classification	Good		Good		Good		Poor		
HC method	$R_c$ (MPa)	41.7–113.0	12	23.5–35.2	11	34.4–42.6	10	4.48–16.0	7
	$K_v$	0.77–1.0	38	0.33–0.72	18	0.36–0.42	35	0.2–0.46	15
	$c$	Non-filling	21	Non-filling	21	Non-filling	21	Mud	6
	$d$	Wet	−1	Wet	−5	Wet	−5	Wet	−7
	$e$	53–67°	−5	85°	−2	80°	−2	60°	−3
	T	50		43		41		18	
	Classification	III		IV		IV		V	

### 3.2. Basic Quality (BQ) Method

“Rock Engineering Classification Standard” (GB/T50218-2014), referred to as the BQ method, provides the necessary foundation for the exploration, design, and quota preparation of rock engineering construction [8]. It combines both qualitative and quantitative methods to determine the quality of rock mass. BQ is measured through two basic properties, i.e., the saturated uniaxial compressive strength  $R_c$  and rock mass integrity coefficient  $K_v$ .  $R_c$  is a good representative of judging the physical and mechanical properties of intact rock.  $K_v$ , which is generally measured by the wave velocity, not only reflects the development degree of the rock mass structural plane but also shows the characteristics of the structural plane. The calculation of  $K_v$  is as follows:

$$K_v = \left( \frac{v_{pm}}{v_{pr}} \right)^2 \quad (5)$$

where  $v_{pr}$  is the vertical wave velocity of intact rock.

The calculation method of BQ based on these two parameters can be written as:

$$BQ = 90 + 3R_c + 250K_v \quad (6)$$

Since various factors have different influences on the quality of rock masses, there should be different weight distributions, so when using the equation, two constraints need to be considered: (1) substituting  $R_c = 90K_v + 30$  into Equation (6) when  $R_c > 90K_v + 30$  and (2) substituting  $K_v = 0.04R_c + 0.4$  into (6) when  $K_v > 0.04R_c + 0.4$ .

In addition, taking into account the influence of groundwater, the occurrence of main weak structural planes, and the initial stress state, the basic quality index BQ of the rock mass should be revised:

$$[BQ] = BQ - 100(K_1 + K_2 + K_3) \quad (7)$$

where  $K_1, K_2, K_3$  is groundwater, the occurrence of main weak structural planes, and initial stress state correction factors, respectively. The results calibrated from the BQ classification system are presented in Table 2.

### 3.3. Hydropower Classification (HC) Method

The advantage of the HC method is that it uses a hierarchical evaluation method. Firstly, intact rock strength, rock mass integrity degree, structural plane conditions, groundwater, and main structural plane attitude are selected as the main correction factors in the HC method. Based on the five factors, the composite index  $T$  can be calculated as:

$$T = a + b + c + d + e \quad (8)$$

where  $a, b, c, d$ , and  $e$  are the ratings of intact rock strength, rock mass integrity degree, structural plane conditions, groundwater, and main structural plane attitude, respectively. Then, the strength-stress ratio of the surrounding rock is used as the limiting criterion to form a constraint evaluation hierarchy, and finally, an integrated surrounding rock quality evaluation method is formed. The strength-stress ratio  $S$  can be calculated with:

$$S = \frac{R_c \cdot K_v}{\sigma_m} \quad (9)$$

where  $\sigma_m$  is the maximum principal stress. This method adopts the method of compulsory downgrading and emphasizes the effect of high stress on the quality of surrounding rock mass. It conforms to the actual situation of the project. The rationality and necessity of this method have been verified in many hydropower projects such as Xiangjiaba, Xiluodu, Wudongde, and Baihetan [24]. The value of HC is also summarized in Table 2.

According to the three rock mass classification methods, the Q system mainly considers the intact rock quality, the development and properties of joints, the influence of

groundwater activity, and the in-situ stress. It emphasizes the integrity of the rock mass. However, there is no direct connection between the strength and deformation characteristics of intact rocks and rock masses. Therefore, the classification results are different from those obtained by the other two classification methods.

This project is located in the area of medium-hard rock and soft rock, with little structural damage and good rock integrity. The developed structural planes are dominated by joints and bedding fissures, and the faults are not developed in the study area. The groundwater is not abundant. The in-situ stress is dominated by the self-weight stress, which is a medium to the low-stress field and has little effect on the conditions of the cavern and the stability of the surrounding rock of the powerhouse. Therefore, the main controlling factors for the stability of the surrounding rock are the strength and deformation of the rock mass itself, the softening characteristics of the soft rock, and the degree of development of structural. Based on the comprehensive three classification methods, combined with the engineering characteristics of the rock mass in the studied area, this project focuses on the HC classification method. The surrounding rock support should focus on factors such as differences in lithology and stress conditions. Based on the HC system composite index  $T$  values, the recommended support categories were determined (Table 3).

**Table 3.** Support measures used in the underground powerhouse based on HC rock mass classification.

Rock Type	Position	Designed Support for the Main Underground Powerhouse (Span B = 25.5 m)
III	Crown	Anchor bolts: $\phi = 25\text{--}32$ , @1.2–1.5 m, $L = 6.0$ m or 9.0 m (9 m for prestressed anchor bolts, and 6 m for conventional anchor bolts), Steel fiber shotcrete $\delta = 20$ cm
	Sidewalls	Anchor bolts: $\phi = 28\text{--}32$ , @1.2–1.5 m, $L = 6.0\text{--}9.0$ m conventional anchor bolts, Steel fiber shotcrete $\delta = 15$ cm, Prestressed anchor cable: @3.0–4.5 m, $L = 15.0\text{--}20.0$ m, $P = 1500\text{--}2000$ KN
IV–V	Crown	Anchor bolts: $\phi = 28\text{--}32$ , @1.0–1.2 m, $L = 6.0$ m or 9.0 m (9 m for prestressed anchor bolts, and 6 m for conventional anchor bolts), Steel fiber shotcrete $\delta = 20$ cm, steel arch or grillage @0.8–1.2 m
	Sidewalls	Anchor bolts: $\phi = 25\text{--}32$ , @1.0–1.2 m, $L = 6.0$ m or 9.0 m (9 m for prestressed anchor bolts, and 6 m for conventional anchor bolts), Steel fiber shotcrete $\delta = 20$ cm, Prestressed anchor cable: @3.0–4.5 m, $L = 20.0\text{--}25.0$ m, $P = 1500\text{--}2000$ KN

### 3.4. Support Design

The Chinese Standard GB 50086-2015 (2015) gives a set of guidelines for the selection of support in the underground powerhouse in rock mass for which the HC value has been defined. Therefore, the schematic diagram of the excavation procedure of the underground powerhouse is determined and shown in Figure 7. The excavation procedure is as follows. Firstly, excavate the ventilation and safety tunnel on the roof of the powerhouse, the traffic tunnel for entering, and the air inlet tunnel of the main powerhouse. After proper support, the main powerhouse and main transformer tunnel are excavated. First, excavate the top arch areas I and II and carry out permanent support, then excavate the III area, and require that the rock anchor crane beam concrete in the III area be completed. After the rock-anchored crane beam concrete reaches the required strength, excavate Zone IV to Zone V (in accordance with the excavation sequence of the plant system, the busbar flat tunnel is Zone IV). To control the large stress and deformation of the plant floor and downstream side walls during the excavation, the construction of Zones VI and VII can only be carried out after the excavation, support, and concrete replacement of Zone VIII have been completed.

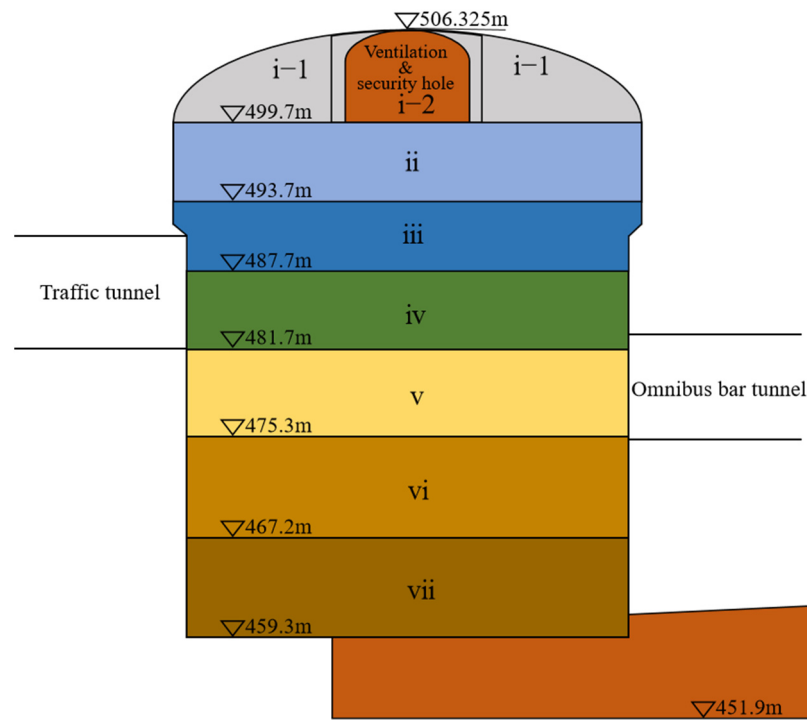


**Figure 7.** Schematic diagram of excavation procedure of underground powerhouse.

#### 4. Numerical Analysis

Nowadays, numerical simulation has been progressively used to check the accuracy of results determined from the empirical method. In continuum modeling, the discontinuities in rock mass are modeled as elements with different material parameters or special joint elements compared with intact rock [25]. Therefore, the materials cannot open or break into pieces and the large deformation of the joint cannot be simulated well. On the other hand, the discrete element method (DEM) which can represent discontinuities explicitly has gained so much attention [26]. The numerical model was built using the DEM through the 3DEC Version 7.0 software package as shown in Figure 8. The cubic three-dimensional model is with dimensions of 140 m × 80 m × 150 m. The model elevation is located at 410 m to 560 m. The model is divided into tetrahedrons, and the minimum unit size is 1.5 m and the maximum unit size is 3.0 m. The total number of elements is 2,132,889 and the total number of nodes is 970,031. There are 5 layers of soft rock in the model, numbered from layer ① to layer ⑤ from top to bottom. The supporting anchor bolts and cables are also presented. The monitoring points B1 to B13 and the points C1 to C7 were set to monitor the stress of bolts and cable force, respectively. 9 monitoring points, namely D1–D9 were set to monitor the deformation during the excavation process.

##### 4.1. Estimation of the Rock Mass Properties

The parameters of rock mass are significantly important to the numerical simulation of excavation. In this paper, the properties of intact rock and discontinuities are combined and represented as rock mass. The strength parameters of rock mass were estimated using the empirical equations suggested by Hoek and Brown [21]. The generalized Hoek-Brown criterion for the estimation of rock mass strength is expressed as,

$$\sigma_1 = \sigma_3 + \sigma_{ci} \left( m_b \frac{\sigma_3}{\sigma_{ci}} + s \right)^a \quad (10)$$

where  $m_b$ ,  $s$  and  $a$  are the rock mass material constants, given by,

$$m_b = m_i \exp[(GSI - 100) / (28 - 14D)] \quad (11)$$

$$s = \exp[(GSI - 100)/(9 - 3D)] \quad (12)$$

$$a = 1/2 + 1/6(e^{-GSI/15} - e^{-20/3}) \quad (13)$$

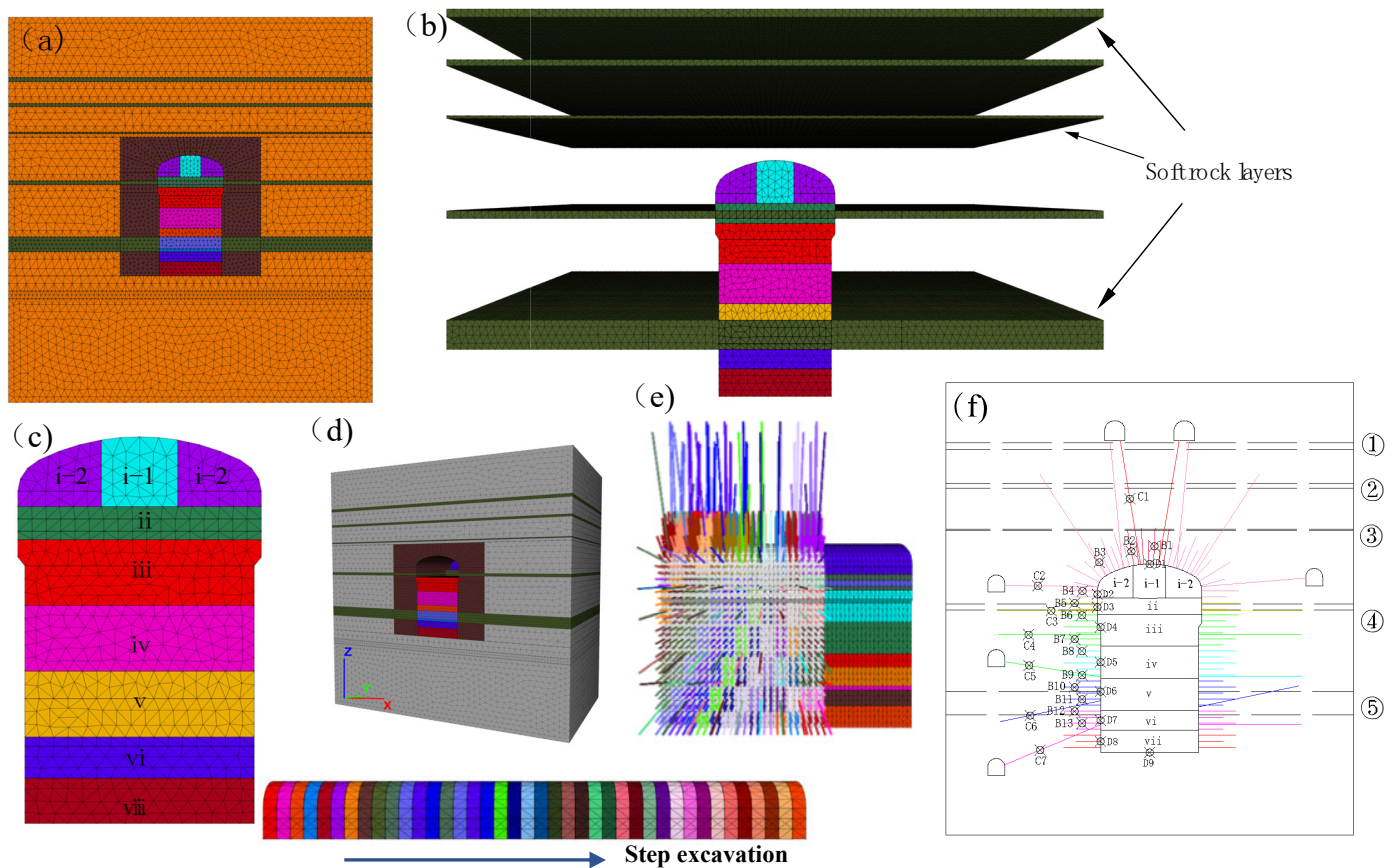


**Figure 8.** Three-dimensional numerical model and set monitoring points: (a) layout of the numerical model; (b) distribution of the soft rock layers; (c) excavation procedure of the underground powerhouse in the z-direction; (d) excavation procedure in the y-direction; (e) Distribution of the supporting anchor bolts and cables and (f) is the monitoring points during the numerical simulation.

The disturbance coefficient  $D$  changes from 0 for undisturbed rock masses to 1 for very poor blasting rock masses. The  $GSI$  (Geological Strength Index) [27] can be estimated from  $BQ$  values with the empirical formulation proposed by Wang et al. [28],

$$GSI = (BQ - 111.24)/6.09 \quad (14)$$

The equivalent stress parameters frictional angle  $\varphi$  and cohesion  $c_{coh}$  based on the Mohr-Coulomb criterion can be determined from the linear part of the Hoek-Brown criterion:

$$\varphi = \sin^{-1} \left[ \frac{6am_b(s + m_b\sigma'_{3n})^{a-1}}{2(1+a)(2+a) + 6am_b(s + m_b\sigma'_{3n})^{a-1}} \right] \quad (15)$$

$$c_{coh} = \frac{\sigma_{ci}[(1+2a)s + (1-a)m_b\sigma'_{3n}](s + m_b\sigma'_{3n})^{a-1}}{(1+a)(2+a)\sqrt{1 + (6am_b(s + m_b\sigma'_{3n})^{a-1})/(1+a)(2+a)}} \quad (16)$$

where  $\sigma'_{3n}$  is a factor related to the maximum confining pressure  $\sigma_{3max}$  and UCS  $\sigma_{ci}$ :  $\sigma'_{3n} = \sigma_{3max}/\sigma_{ci}$ . The physical and mechanical properties of the rock masses are shown in Table 4. The interface and discontinuities are described by the Coulomb Slip model and the

mechanical parameters are estimated by the method suggested by Kulatilake [29,30] (as shown in Table 5).

**Table 4.** Physical and mechanical properties of rock mass in the numerical model.

Rock Class	Lithology	$\rho$ (kg/m <sup>3</sup> )	$E_m$ (GPa)	$\mu_m$	$c_{coh}$ (MPa)	$\varphi$ (°)
III	Sandstone	2650	14.90	0.21	0.92	44.4
IV	Conglomerate, Siltstone	2500	6.55	0.24	0.35	32.6
V	Mudstone	2490	0.5	0.30	0.1	19.3

**Table 5.** Mechanical property values used for discontinuities in the numerical model.

Normal Stiffness $K_N$ (GPa/m)	Shear Stiffness $K_s$ (GPa/m)	Frictional Angle $\varphi'$ (°)	Cohesion $c'$ (MPa)
$4.0 \times 10^9$	$2.5 \times 10^9$	25.0	0.1

The supports used are cable bolt elements as available in 3DEC. Table 6 gives the material property values of the bolt in the numerical model with a diameter of 32 mm. The material property values of bolts with other diameters ( $\Phi = 25$  mm and 28 mm) can be calculated as follows. The left three parameters in Table 6 were estimated based on the information provided by the electric power company, the manufacturers, and the suggestions given in the manual of 3DEC. The grout annulus thickness  $t$  is equal to 20 mm and the grout shear modulus  $G$  is 9 GPa. In many cases, the grout stiffness is hard to determine, and the following equation is usually used to provide a reasonable estimation of the program:

$$k_g \simeq \frac{2\pi G}{10 \ln(1 + 2t/\vartheta)} \quad (17)$$

where  $\vartheta$  is cable diameter and  $k_g$  is the grout stiffness. The grout exposed perimeter is expressed as  $p_g = \pi(\vartheta + 2t)$ .

**Table 6.** Material property values used for rock supports in the numerical model ( $\Phi = 32$  mm).

Young's Modulus (GPa)	Grout Friction Angle (deg)	Grout Cohesive Strength (kN/m)	Grout Stiffness (GN/m <sup>2</sup> )	Grout Exposed Perimeter (m)	Cable Cross-Sectional Area (m <sup>2</sup> )
210	28.0	800	6.37	0.226	$8.04 \times 10^{-4}$

According to the in-situ stress test results, the vertical in-situ stress is mainly the self-weight of the rock mass. Therefore, the vertical stress was estimated from:

$$\sigma_v = \gamma H \quad (18)$$

where  $\gamma$  is the average unit weight of rock mass, and  $H$  is overburden thickness. The tested horizontal stress coefficient is between 0.46 and 0.63. The average value of 0.55 is selected for numerical simulation.

#### 4.2. Numerical Simulation Results

Following the field excavations and supporting procedures, the underground powerhouse was excavated and supported in seven steps. The maximum principal stress distribution during the step construction under unsupported conditions is shown in Figure 9. The results show that the excavation-induced unloading of the surrounding rock mass leads to variations in the maximum principal stresses. Within the surrounding rock mass, stress zones of both relaxation and focus are created. The area of stress concentration slowly travels to the interior of the surrounding rock mass as excavation work progresses.

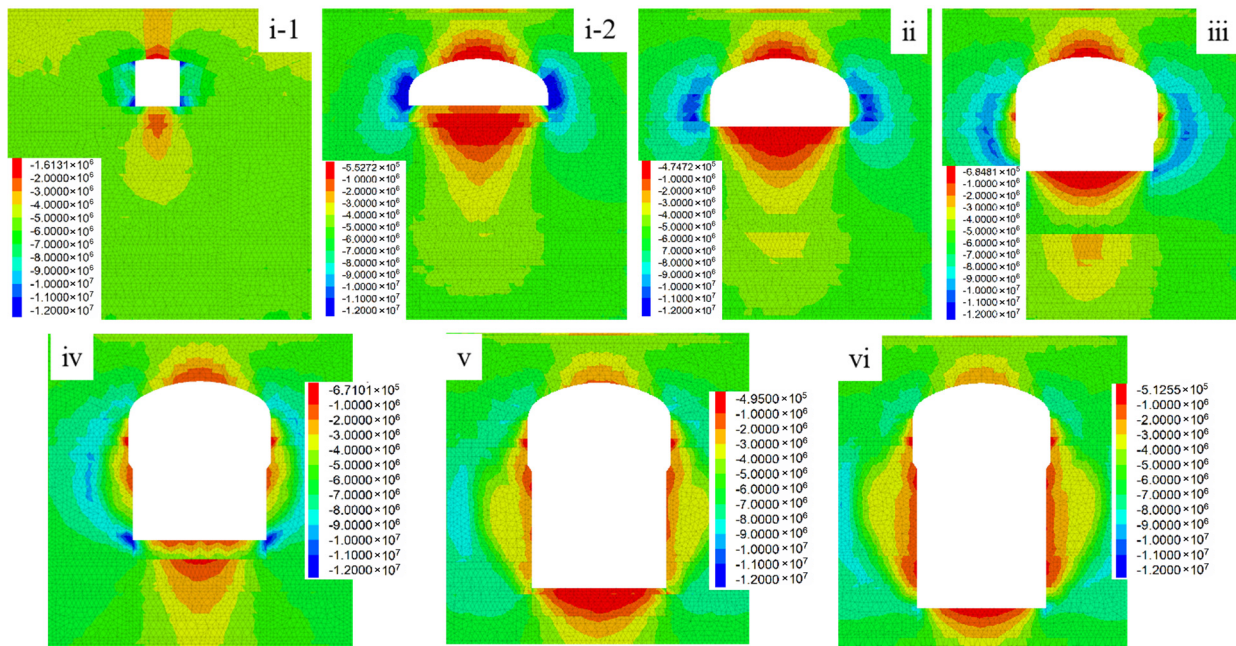


Figure 9. Stress distributions during the step construction of the underground powerhouse.

The stress distributions after the final step of the excavation are shown in Figure 10. It is obvious that the maximum principal stress distribution under the two support conditions is the same. The maximum values are all concentrated at the bottom of the sidewall. The installation of bolts and cables increases the support stability of the rock. Therefore, the stresses of the downside of the sidewalls and crown increase. In particular, the stress of soft rock layers ④ and ⑤ increases significantly in these areas.

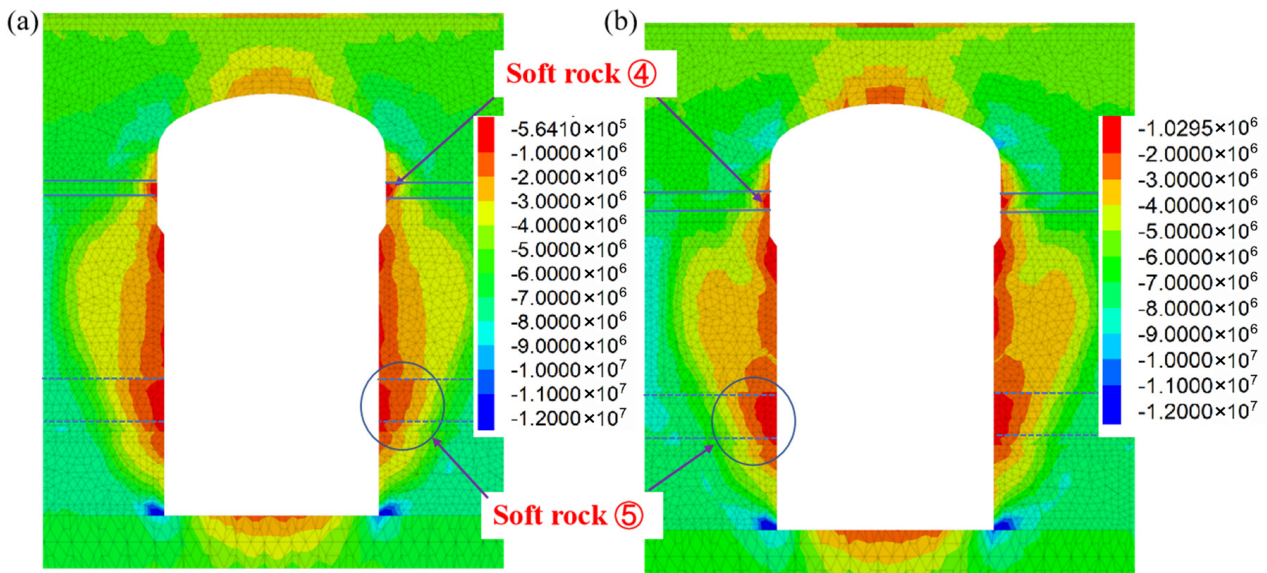
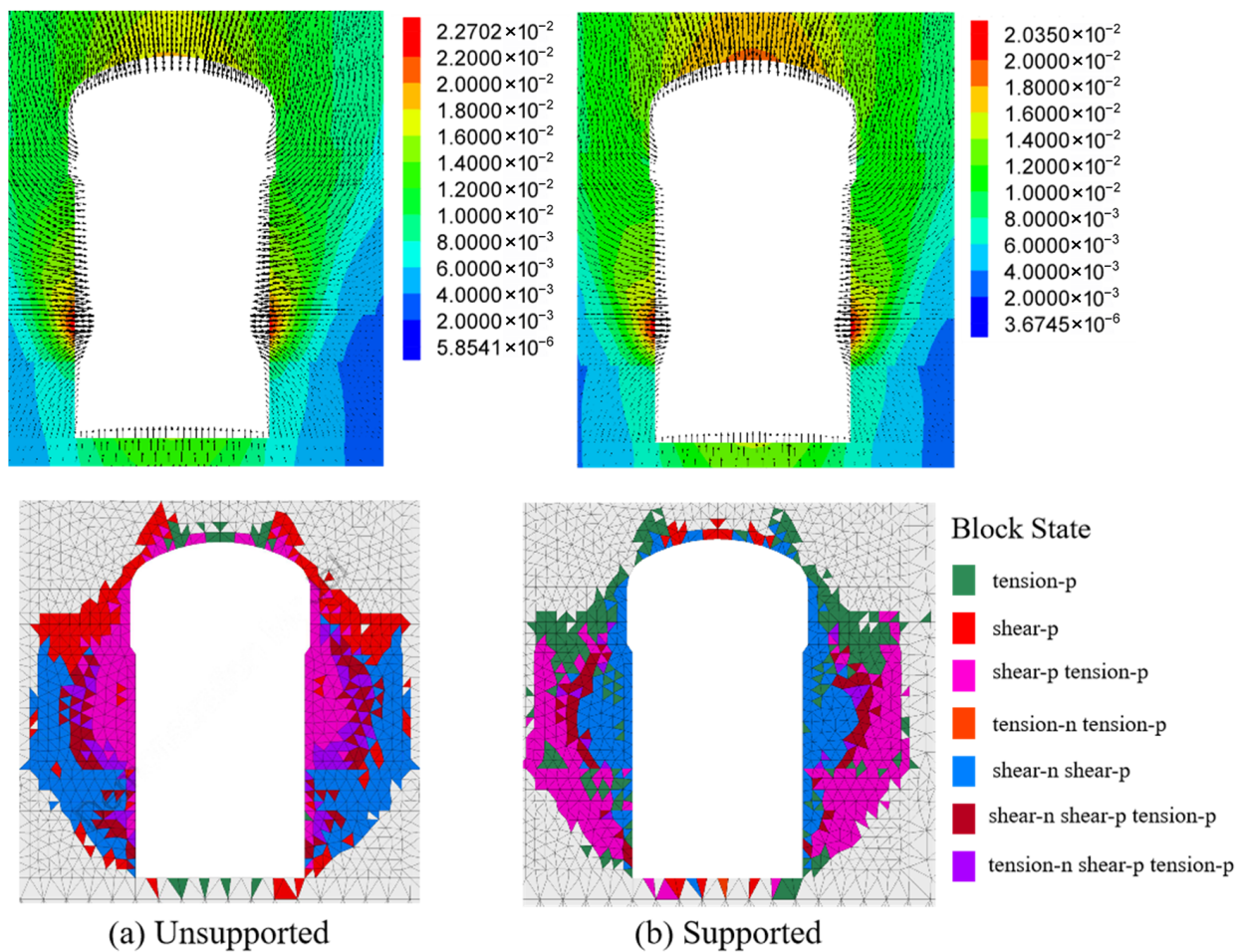


Figure 10. Stress distributions after the final step of the excavation: (a) unsupported and (b) supported.

The developed deformation and plastic zone were assessed based on the numerical simulation results. The maximum deformation and plastic zone after each excavation step for both supported and unsupported cases are given in Table 7 and Figure 11.

**Table 7.** Numerical results for the main powerhouse of Panlong pumped-storage power station.

Monitoring Point	Position	Maximum Displacement (mm)		Radius of Plastic Zone (m)	
		Unsupported Case	Supported Case	Unsupported Case	Supported Case
D1	Crown (i)	17.3	16.8	2.0	2.0
D2	Skewback (ii)	11.2	11.1	3.0	3.0
D3	Sidewall (iii, mudstone)	11.8	12.3	3.0	3.0
D4	Sidewall (iii)	12.6	11.0	4.0	4.0
D5	Sidewall (iv)	14.9	12.8	7.0	5.0
D6	Sidewall (v, mudstone)	21.4	18.7	12.0	11.0
D7	Sidewall (vi)	8.2	7.1	14.0	13.0
D8	Sidewall (vii)	6.7	6.3	14.0	13.0
D9	Floor	13.3	13.1	2.0	2.0



**Figure 11.** Maximum total displacement and plastic zone thickness under (a) unsupported and (b) supported conditions.

Under the supported case, the overall displacement of each monitoring point is basically reduced compared to the under-supported case. The support has distinct restraint effects on the excavation deformation of the iii layer to the vii layer. Particularly, the displacement of the D6 monitoring point located in the soft rock part of the layer ⑤ is significantly reduced under the supported case, and the reduction value is 2.7 mm. Supporting has a certain inhibitory effect on the development of the plastic zone of the surrounding rock during the excavation process below the iv layer, and the restraint effect on the iv layer is the most obvious. Under the supported case, the thickness of the plastic zone of the surrounding rock is reduced by almost 2 m.

Figure 12 shows the horizontal dislocation of soft rock bedding in under-supported and unsupported cases. It shows that after the excavation of layer viii, the soft rock layer ⑤ has a horizontal displacement of 3.7 mm under the unsupported case. Under the support condition, the amount of horizontal misalignment reduces to 2.3 mm, which is about 37.8%. It shows that the supporting setup has obvious effects on limiting the slippage of soft rock.

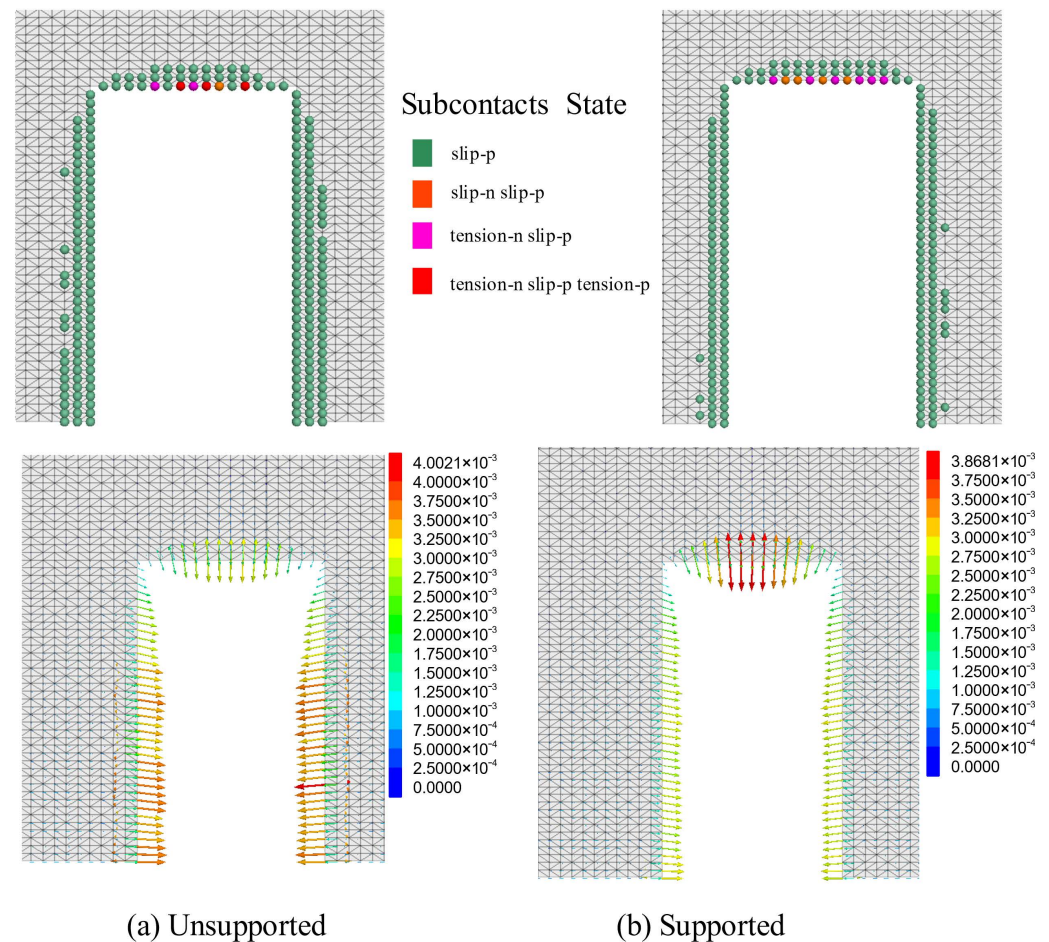


**Figure 12.** Joint shear state and displacement vectors along with the soft rock layer ⑤ under (a) unsupported and (b) supported conditions.

Figure 13 shows the stress distribution diagram of the anchor bolt after excavation. After the excavation of the iii layer, the tensile stress of the bolt at the top arch has no obvious change, and the maximum value is about 30 MPa. Since the excavation of the v layer, the stress of the bolt at the sidewall increases obviously with the excavation of layer by layer. After the excavation of the viii layer, the stress of the bolt at the monitoring point of the side wall reaches about 150 MPa.

Figure 14 is the stress distribution diagram of prestressed anchor cable after excavation. According to the support design, the initial prestress applied to the anchor cable is 2000 KN. During the excavation process, the tensile stress value of the anchor cable increases gradually with the increase of the number of layers excavated, but the increase is not large. After the excavation of layer vii, the maximum tensile stress of the prestressed anchor cable appears at the left side wall of the iv, and the maximum tensile stress value is 2242 KN. It is higher than the initial value, with an increase of 12.1%. It can be seen from the above analysis that anchor bolts and cables have a good constraint on the deformation of an underground powerhouse. At the same time, the stress distribution of the anchor bolts and anchor cables is within its design value, which indicates that the supporting design

method suggested by HC surrounding rock classification method can meet the stability requirements of an underground powerhouse.

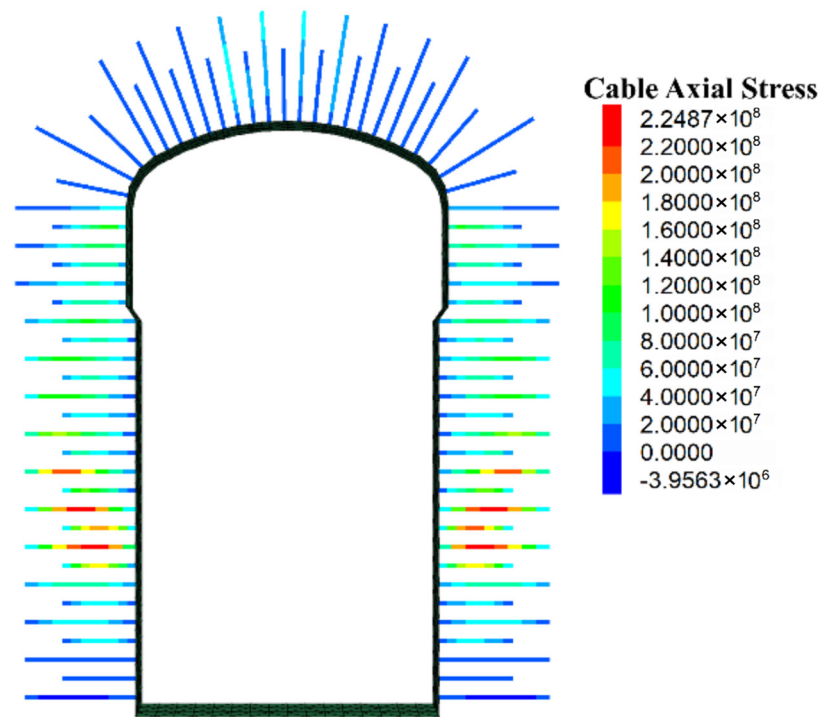


Figure 13. Anchor bolts stress distribution after excavation.

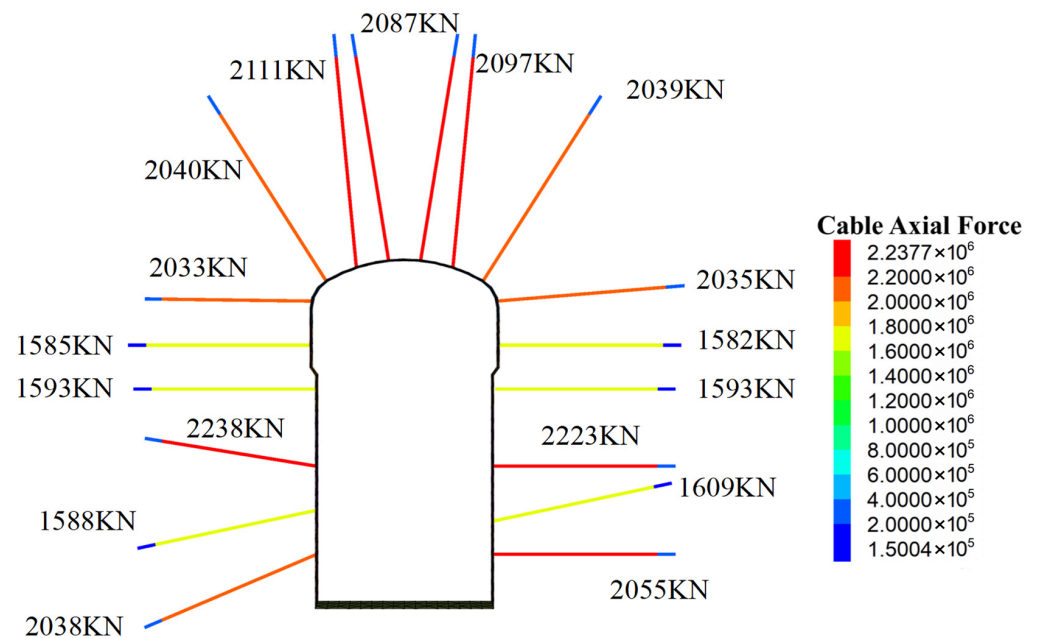
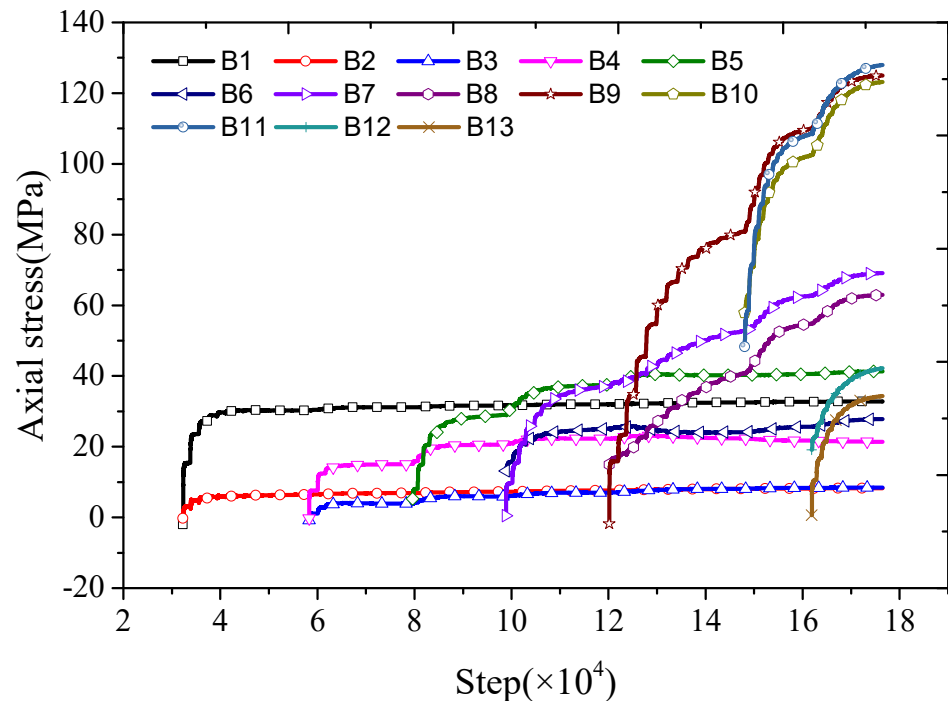


Figure 14. Axial force distribution of prestressed anchor cable after excavation.

#### 4.3. Compared with Monitoring Results

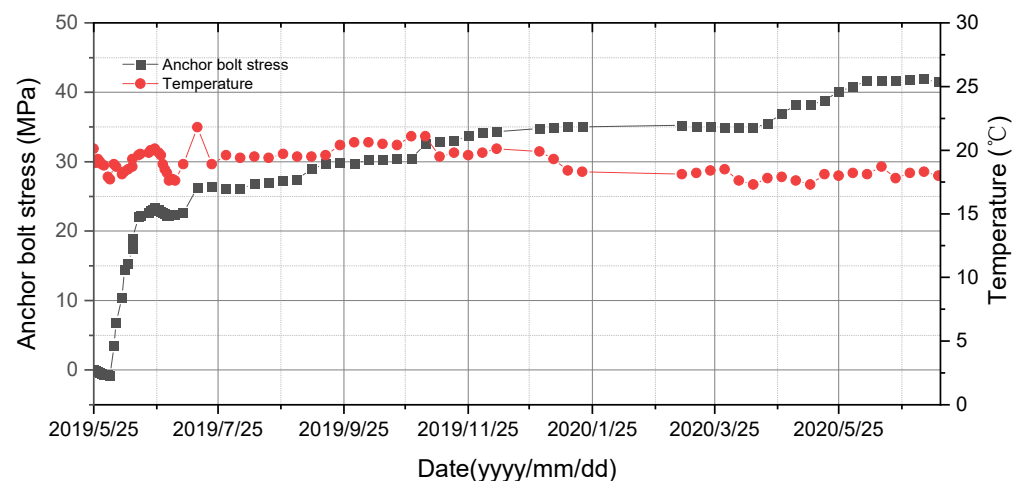
Furthermore, the FISH language in 3DEC was used to record the change process of the average stress of the bolt at the monitoring site during the layered excavation. Figure 15 shows the average stress change histogram of bolts numbered B1–B13. It can be seen from the figure that the tensile stress of the bolts numbered B1–B4 at the top arch has basically no obvious change after the excavation of the third layer. Among them, the stress of the B1

numbered anchor is the largest, and the maximum value is about 30 MPa. Starting from the excavation of the v layer, with the layer-by-layer excavation, the stress of the B9–B11 numbered anchors at the side wall has increased significantly. After the excavation of the vii layer, the bolt stress at the B11 monitoring point reached about 130 MPa.



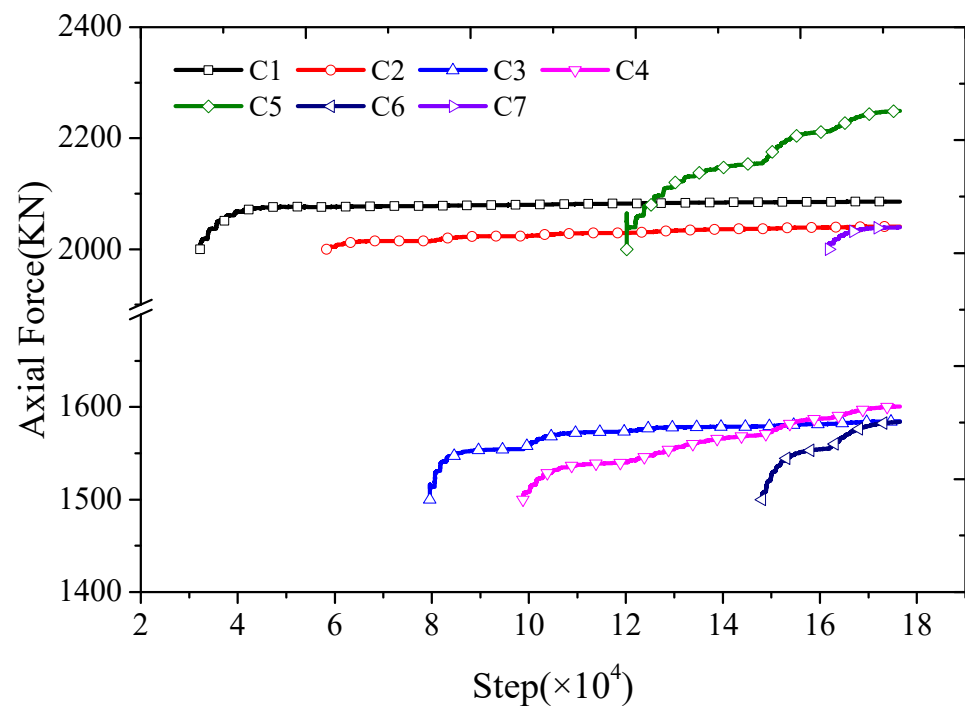
**Figure 15.** Change of average bolt stress in different monitoring positions during layered excavation.

Figure 16 shows the monitoring results of the anchor bolt stress gauge at the top arch during the excavation of the i–iii floors of the main powerhouse (B1). From the results of on-site monitoring, as the excavation progresses, the axial force of the bolt rapidly increases to about 25 MPa. After that, the axial force of the bolt increases slowly with the excavation, and the monthly variation is about 1.5 MPa. Comparing Figures 15 and 16, it can be seen that the numerical simulation results of the excavation of layers i to iii are relatively close to the monitoring results of B1 at the same monitoring site. The correctness of the numerical model is further verified.



**Figure 16.** Bolt stress gauge monitoring results of B1.

Two types of anchor cables are used in this program. One with a prestress of 1500 KN (C3, C4, and C6) and the other with a prestress of 2000 KN (thru-anchor cables, C1, C2, C5, and C7) as shown in Figure 9. Figure 17 shows the change of the anchor cable force at each monitoring position during the layered excavation process. During the excavation process layer by layer, the force value of the anchor cable is increasing continuously. The stress value of the anchor cable at the side wall of the iv layer has a relatively large increase, and the increased value is about 250 KN. After the excavation of the first floor, the anchor cable stress at the monitoring position C1 at the top of the vault is basically at a stable value. Compared with the initial value, its value increased by about 100 KN, and the increase was not large.



**Figure 17.** Change of average anchor cable force in different monitoring positions during layered excavation.

The typical prestressed anchor cable installed corresponds to the place near C3 is shown in Figure 18. It can be seen that the variation of the anchor cable force is between 1430 to 1490 KN. Judging from the current monitoring results of the powerhouse anchor cables, the main powerhouse has installed anchor cable dynamometers with loads ranging from 1337.46 KN to 1512.32 KN, with monthly changes ranging from  $-1.73$  KN to 1.67 KN, with little change. It is basically consistent with the numerical simulation results of the excavation of layers i to iii. Therefore, the supporting method used in this program is reasonable.

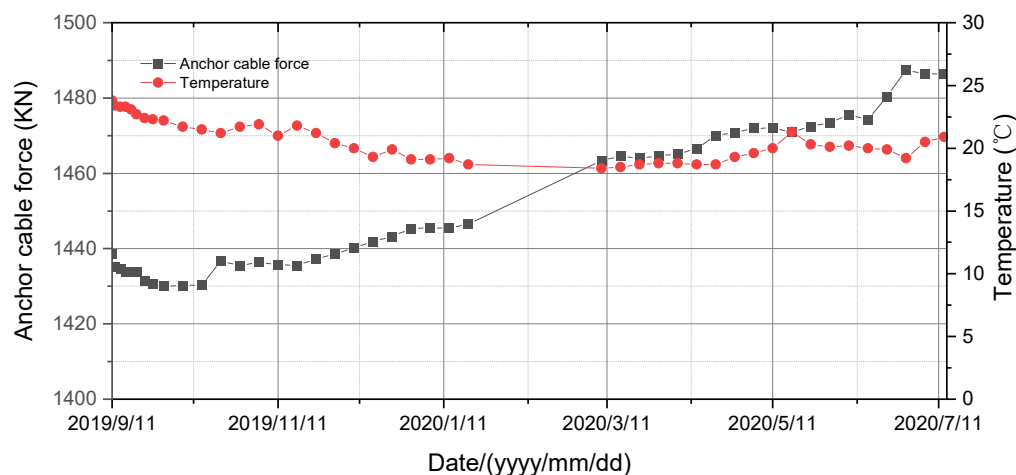


**Figure 18.** Monitoring results of DPA-3 prestressed anchor cable (correspond to position C3).

## 5. Conclusions

In this paper, field and laboratory tests were conducted to investigate the geology situation of the underground powerhouse of pumped-storage power station in Chongqing, China. Three empirical rock mass classification methods were utilized to evaluate the quality of rock mass in the site and the corresponding support system was developed subsequently. The three-dimensional DEM-based software programs were used to check the efficiency of the empirical support system. The main conclusions are as follows

- (1) The lithology of the underground powerhouse is mainly composed of sandstone, conglomerate, and Siltstone. The rock masses have geological conditions for cave formation, and the overall stability of the surrounding rock mass is good. But below the elevation of 469.89–476.60 m and the elevation of the arch above 506.325 m, mudstone is distributed. The rock strength is low and the ability to resist deformation is poor. In addition, the cavern has a large span, so the surrounding rock is prone to instability after excavation, and it must be supported in time.
- (2) The main controlling factors for the stability of the surrounding rock are the strength and deformation of the rock mass itself, the softening characteristics of the soft rock, and the degree of development of structural. Based on the comprehensive qualification of the Q classification system, basic quality (BQ) method, and hydropower classification (HC) method, the HC classification method was used to determine the support system, and the excavation procedure was proposed accordingly.
- (3) The support system can effectively reduce the deformation and plastic zone during the excavation of the underground powerhouse. In addition, the supporting setup has obvious effects on limiting the slippage of the soft rock layers. In general, the empirical classification methods and numerical methods are useful tools for preliminary assessments of large-span underground powerhouse support designs.

**Author Contributions:** Data curation, Y.Z.; formal analysis, Q.Z.; funding acquisition, Q.Z. and Y.Z.; investigation, Y.Z.; methodology, Y.Z.; software, Q.Z.; validation, Y.Z.; writing—original draft, Y.Z.; writing—review and editing, Q.Z. and Y.Z. All authors have read and agreed to the published version of the manuscript.

**Funding:** This research was funded by the National Key R&D Program of China (Grant No. 2018YFC0407006), the National Natural Science Foundation of China (Grant No. U1934211), National Natural Science Foundation of China-Yalong River Joint Fund Key Project (Grant No. U1965204) and the Central South University Autonomous Exploration Project (No. 2021zzts0233).

**Institutional Review Board Statement:** Not applicable.

**Informed Consent Statement:** Not applicable.

**Data Availability Statement:** All data, models, and code that support the findings of this study are available from the corresponding author upon reasonable request.

**Conflicts of Interest:** The authors declare no conflict of interest.

#### List of Symbols:

$E_m$	Deformation modulus of rock mass
$E_{me}$	Elastic modulus of rock mass
$R_c$	Uniaxial compressive strength
$\nu$	Poisson's ratio of intact rock
$\mu_m$	Poisson's ratio of rock mass
$p$	Pressure applied on the rigid bearing plate
$b$	Diameter of the rigid bearing plate
$W$	Total deformation of rock mass during rigid bearing plate test
$\theta$	A coefficient related to the stiffness and shape of the rigid bearing plate
$D$	A coefficient describing the disturbance degree of the rock mass subject to blast damage and stress relaxation
$GSI$	Geological strength index
$v_{pm}$	Seismic vertical wave velocity
$v_{sm}$	Seismic horizontal wave velocity
$J_n$	Number of joint sets
$J_r$	Joint roughness number
$J_a$	Joint alteration number
$J_w$	Joint water reduction factor
$SRF$	Stress reduction factor
$K_v$	Rock mass integrity coefficient
$v_{pr}$	Vertical wave velocity of intact rock
$K_1, K_2, K_3$	Groundwater, the occurrence of main weak structural planes, and initial stress state correction factors
$a, b, c, d, \text{ and } e$	The ratings of intact rock strength, rock mass integrity degree, structural plane conditions, groundwater, and main structural plane attitude,
$S$	Strength-stress ratio
$\sigma_m$	Maximum principal stress
$m_b, s, \sigma_{ci}, \alpha$	Parameters related to the Hoek-Brown criterion for rock mass
$m_i$	Material constant related to Hoek-Brown criterion for intact rock
$\varphi, c_{coh}$	Frictional angle and cohesion based on Mohr-Coulomb criterion
$\sigma'_{3n}$	A factor related to the maximum confining pressure and UCS
$\sigma_v$	Vertical in-situ stress
$\gamma$	Average unit weight of rock mass
$H$	Overburden thickness.
$K_N, K_s$	Normal stiffness and shear stiffness of discontinuities
$\varphi', c'$	Frictional angle and cohesion of discontinuities

#### References

- Jia, C.J.; Xu, W.Y.; Wang, R.B.; Wang, S.S.; Lin, Z.N. Experimental investigation on shear creep properties of undisturbed rock discontinuity in Baihetan Hydropower Station. *Int. J. Rock Mech. Min. Sci.* **2018**, *104*, 27–33. [[CrossRef](#)]
- Sebbeh-Newton, S.; Shehu, S.A.; Ayawah, P.; Kaba, A.A.; Zabidi, H. Analytical and numerical assessment of a preliminary support design—A case study. *Cogent Eng.* **2021**, *8*, 1869367. [[CrossRef](#)]
- Rehman, H.; Naji, A.M.; Ali, W.; Junaid, M.; Abdullah, R.A.; Yoo, H.K. Numerical evaluation of new Austrian tunneling method excavation sequences: A case study. *Int. J. Min. Sci. Technol.* **2020**, *30*, 381–386. [[CrossRef](#)]
- Yalcin, E.; Gurocak, Z.; Ghabchi, R.; Zaman, M. Numerical Analysis for a Realistic Support Design: Case Study of the Komurhan Tunnel in Eastern Turkey. *Int. J. Geomech.* **2016**, *16*, 05015001. [[CrossRef](#)]
- Wickham, G.; Tiedemann, H.; Skinner, E. Support determinations based on geologic predictions. In Proceedings of the North American Rapid Excavation and Tunnelling Conference, Chicago, IL, USA, 5–7 June 1972.
- Bieniawski, Z.T. Engineering rock mass classifications: A complete manual for engineers and geologists in mining, civil, and petroleum engineering. In *Engineering Rock Mass Classifications*; John Wiley & Sons: New York, NY, USA, 1989.
- Barton, N.; Lien, R.; Lunde, J. Engineering classification of rock masses for the design of tunnel support. *Rock Mech.* **1974**, *6*, 189–236. [[CrossRef](#)]
- GB/T50218-2014*; Standard for Engineering Classification of Rock Masses. China Planning Press: Beijing, China, 2014.
- GB 50086-2015*; Technical Code for Engineering of Ground Anchorages and Shotcrete Support. China Planning Press: Beijing, China, 2015.
- Xing, Y.; Kulatilake, P.H.S.W.; Sandbak, L.A. Effect of rock mass and discontinuity mechanical properties and delayed rock supporting on tunnel stability in an underground mine. *Eng. Geol.* **2018**, *238*, 62–75. [[CrossRef](#)]

11. Xing, Y.; Kulatilake, P.H.S.W.; Sandbak, L.A. Stability Assessment and Support Design for Underground Tunnels Located in Complex Geologies and Subjected to Engineering Activities: Case Study. *Int. J. Geomech.* **2019**, *19*, 05019004. [[CrossRef](#)]
12. Yang, S.Q.; Chen, M.; Jing, H.W.; Chen, K.F.; Meng, B. A case study on large deformation failure mechanism of deep soft rock roadway in Xin'An coal mine, China. *Eng. Geol.* **2017**, *217*, 89–101. [[CrossRef](#)]
13. Kanik, M.; Gurocak, Z. Importance of numerical analyses for determining support systems in tunneling: A comparative study from the trabzon-gumushane tunnel, Turkey. *J. Afr. Earth Sci.* **2018**, *143*, 253–265. [[CrossRef](#)]
14. Jia, C.; Xu, W.; Wang, S.; Wang, R.; Yu, J. Experimental analysis and modeling of the mechanical behavior of breccia lava in the dam foundation of the Baihetan Hydropower Project. *Bull. Eng. Geol. Environ.* **2018**, *78*, 2681–2695. [[CrossRef](#)]
15. Zhang, Q.; Jia, C.J.; Yu, J.; Zhou, J.W. Multisphere Representation of Convex Polyhedral Particles for DEM Simulation. *Adv. Civ. Eng.* **2021**, *2021*, 8846004. [[CrossRef](#)]
16. Yuan, C.; Su, C. Structural characteristics of Panlong underground powerhouse considering excavation of all caverns. *Adv. Sci. Technol. Water Resour.* **2018**, *38*, 56–61.
17. ISRM. *The ISRM Suggested Methods for Rock Characterization, Testing and Monitoring: 2007–2014*; Springer: Berlin/Heidelberg, Germany, 2014.
18. Priest, S.D.; Hudson, J.A. Discontinuity spacings in rock. *Int. J. Rock Mech. Min. Sci. Geomech. Abstr.* **1976**, *13*, 135–148. [[CrossRef](#)]
19. DZ/T 0276.26-2015; Regulation for Testing the Physical and Mechanical Properties of Rock-Part 26: Test for Determining the Deformation of Rock Mass (Bearing Plate Method). China Planning Press: Beijing, China, 2015.
20. Xing, Y.; Kulatilake, P.H.S.W.; Sandbak, L.A. Investigation of Rock Mass Stability Around the Tunnels in an Underground Mine in USA Using Three-Dimensional Numerical Modeling. *Rock Mech. Rock Eng.* **2017**, *51*, 579–597. [[CrossRef](#)]
21. Hoek, E.; Brown, E.T. The Hoek-Brown failure criterion and GSI-2018 edition. *J. Rock Mech. Geotech. Eng.* **2019**, *11*, 445–463. [[CrossRef](#)]
22. Liu, Q.S.; Liu, J.P.; Pan, Y.C.; Kong, X.X.; Hong, K.R. A case study of TBM performance prediction using a Chinese rock mass classification system—Hydropower Classification (HC) method. *Tunn. Undergr. Space Technol.* **2017**, *65*, 140–154. [[CrossRef](#)]
23. Hudson, J.A.; Cornet, F.H.; Christiansson, R. ISRM suggested methods for rock stress estimation-part 1: Strategy for rock stress estimation. *Int. J. Rock Mech. Min. Sci.* **2003**, *40*, 991–998. [[CrossRef](#)]
24. Jiang, Q.; Feng, X.T.; Hatzor, Y.H.; Hao, X.J.; Li, S.J. Mechanical anisotropy of columnar jointed basalts: An example from the Baihetan hydropower station, China. *Eng. Geol.* **2014**, *175*, 35–45. [[CrossRef](#)]
25. Jing, L. A review of techniques, advances and outstanding issues in numerical modelling for rock mechanics and rock engineering. *Int. J. Rock Mech. Min. Sci.* **2003**, *40*, 283–353. [[CrossRef](#)]
26. Shreedharan, S.; Kulatilake, P.H.S.W. Discontinuum-Equivalent Continuum Analysis of the Stability of Tunnels in a Deep Coal Mine Using the Distinct Element Method. *Rock Mech. Rock Eng.* **2016**, *49*, 1903–1922. [[CrossRef](#)]
27. Hoek, E.; Kaiser, P.; Bawden, W. *Support of Underground Excavations in Hard Rock*; AA Balkema: Rotterdam, The Netherlands, 1995; pp. 84–97.
28. Wang, M.N.; Wang, Z.L.; Tong, J.J.; Zhang, X.; Dong, Y.C.; Liu, D.G. Support pressure assessment for deep buried railway tunnels using BQ-index. *J. Cent. South. Univ.* **2021**, *28*, 247–263. [[CrossRef](#)]
29. Kulatilake, P.H.S.W.; Park, J.; Um, J.-G. Estimation of rock mass strength and deformability in 3-D for a 30 m cube at a depth of 485 m at Äspö Hard Rock Laboratory. *Geotech. Geol. Eng.* **2004**, *22*, 313–330. [[CrossRef](#)]
30. Kulatilake, P.H.S.W.; Wang, S.; Stephansson, O. Effect of finite size joints on the deformability of jointed rock in three dimensions. *Int. J. Rock Mech. Min. Sci. Geomech. Abstr.* **1993**, *30*, 479–501. [[CrossRef](#)]